Filament Frontogenesis by Boundary Layer Turbulence

JAMES C. MCWILLIAMS, JONATHAN GULA, M. JEROEN MOLEMAKER, LIONEL RENAULT, AND ALEXANDER F. SHCHEPETKIN

Institute of Geophysics and Planetary Physics, University of California, Los Angeles, Los Angeles, California

(Manuscript received 14 October 2014, in final form 4 May 2015)

ABSTRACT

A submesoscale filament of dense water in the oceanic surface layer can undergo frontogenesis with a secondary circulation that has a surface horizontal convergence and downwelling in its center. This occurs either because of the mesoscale straining deformation or because of the surface boundary layer turbulence that causes vertical eddy momentum flux divergence or, more briefly, vertical momentum mixing. In the latter case the circulation approximately has a linear horizontal momentum balance among the baroclinic pressure gradient, Coriolis force, and vertical momentum mixing, that is, a turbulent thermal wind. The frontogenetic evolution induced by the turbulent mixing sharpens the transverse gradient of the longitudinal velocity (i.e., it increases the vertical vorticity) through convergent advection by the secondary circulation. In an approximate model based on the turbulent thermal wind, the central vorticity approaches a finite-time singularity, and in a more general hydrostatic model, the central vorticity and horizontal convergence are amplified by shrinking the transverse scale to near the model's resolution limit within a short advective period on the order of a day.

1. Introduction

A widespread appreciation has emerged and grown in the past several years for how active the regime of submesoscale currents is within the oceanic surface layer. Examples are density fronts and filaments, their instabilities, coherent vortices, vertical material fluxes, and a forward energy cascade to an enhanced dissipation rate. Mesoscale eddies are the energy source for submesoscale flows and density gradients, and strain-induced frontogenesis is a process that can shrink the horizontal scale of density gradients at a super-exponential rate. Fronts—a transverse horizontal step in surface density across an elongated longitudinal axis—have a long history of investigation, both dynamically (Hoskins 1982) and observationally (e.g., Rudnick and Luyten 1996; Rudnick 1996). Filaments—a transverse horizontal extremum in surface density—have analogous dynamical processes (Hakim et al. 2002; Lapeyre and Klein 2006; McWilliams et al. 2009b) but have perhaps less often been observed; examples are detection in satellite images (e.g., probably the spiral arms in cyclonic surface vortices; Munk et al. 2000) and the ''streamers'' documented in Rudnick and Luyten (1996). Because of the central surface convergence and downwelling in the strain-induced secondary circulation (Fig. 1), dense filaments have a stronger frontogenetic rate than do fronts, and light filaments have a reverse secondary circulation, hence an even weaker frontogenetic rate, and thus are likely to be weaker and rarer in the ocean. Both fronts and filaments are subject to rotating, stratified, momentum-balanced (i.e., barotropic and baroclinic) instabilities with finite longitudinal wavenumbers (McWilliams et al. 2009a; Gula et al. 2014).

An outstanding question is how frontogenesis is arrested at some finite horizontal scale while the straining deformation persists; if it is not by one of the balanced instabilities (McWilliams and Molemaker 2011), then it might be by other smaller-scale instabilities as part of the boundary layer turbulence. When the turbulent flux is parameterized with a finite horizontal eddy viscosity, then of course an arrest might occur diffusively, but this is just a surrogate for the true arrest process.

Most theoretical studies of fronts and filaments have been made with conservative dynamics; that is, less attention has been given to the effect of the surface boundary layer turbulence that usually occurs simultaneously. Garrett and Loder (1981) determines an

Corresponding author address: James C. McWilliams, IGPP, UCLA, Los Angeles, CA 90095-1567.
E-mail: jcm@atmos.ucla.edu

DOI: 10.1175/JPO-D-14-0211.1

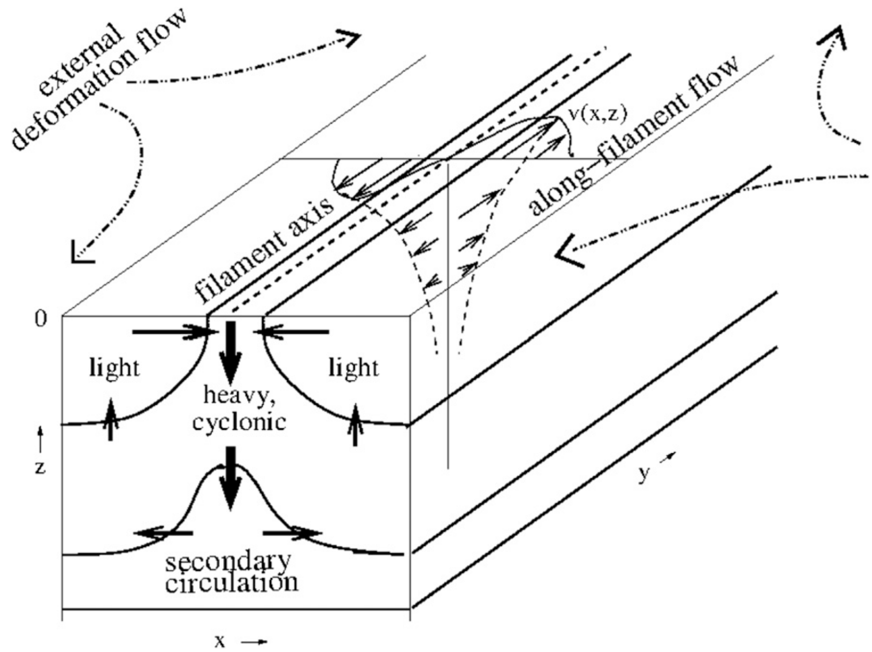

FIG. 1. Sketch of a two-dimensional dense surface filament undergoing frontogenesis in an external horizontal deformation flow with uniform horizontal strain rate ($\partial_x u - \partial_y v$; dotted–dash arrows). Buoyancy contours [$b(x, z) = g(\rho_0 - \rho)/\rho_0$; heavy solid lines] bulge up in the center, as labeled by "light" and "heavy." The approximately geostrophic longitudinal flow v (thin arrows) is a double jet. The ageostrophic secondary circulation (u, w) in the transverse plane (thick arrows) has central downwelling and peripheral upwelling, surface horizontal convergence, and subsurface horizontal divergence. Vortex stretching generates cyclonic vertical vorticity in the center and weaker anticyclonic vorticity on the edges. (Adapted from McWilliams et al. 2009b.)

approximate secondary circulation due to vertical mixing[1] near a front and shows that it leads to a diffusive horizontal relaxation of the tilted isopycnal depths with, however, some local frontogenetic sharpening due to nonuniform stratification or eddy viscosity. Nagai et al. (2006) shows how the frontal secondary circulation pattern and strength vary with the vertical mixing parameters. Thomas and Lee (2005) shows that the vertical mixing associated with a down-front wind has a frontogenetic effect through the secondary circulation.

In the absence of nonconservative mixing or straining deformation, an isolated filament, once formed, can be in a hydrostatic, geostrophic, and stationary state. This paper is a study of the evolution of an isolated, two-dimensional (2D), dense filament due to the boundary layer turbulence from surface wind stress and parameterized as the vertical mixing of buoyancy and momentum. The result is that the vertical mixing itself causes a further horizontal frontogenesis through the induced secondary circulation, which continues (in this 2D model) down to an arrest by the modeled diffusion at an approximately isotropic aspect ratio with the transverse scale comparable to the boundary layer depth.

In the following sections, an illustration is presented of filament buoyancy structure, vertical mixing, and circulation from a realistic oceanic simulation (section 2); turbulent thermal wind balance is defined and solved (section 3); an idealized filament with turbulent thermal wind balance and its implied frontogenetic tendency are evaluated (section 4); the time evolution of an idealized filament is solved for and analyzed (section 5); an approximate, balanced model of filament frontogenesis is educed that exhibits a finite-time singularity (section 6); and the results are summarized with an additional discussion of future research directions (section 7).

[1] Small-scale turbulence causes both horizontal and vertical eddy fluxes (i.e., mixing), of course. However, if the density and circulation structure has a small vertical/horizontal aspect ratio, while the turbulence is more nearly isotropic, then the horizontal mixing will have a much smaller effect on the structure. If frontogenesis occurs in such a way as to increase the aspect ratio, then at some time the horizontal mixing may become important, but this latter phase is not investigated in this paper (section 5b).

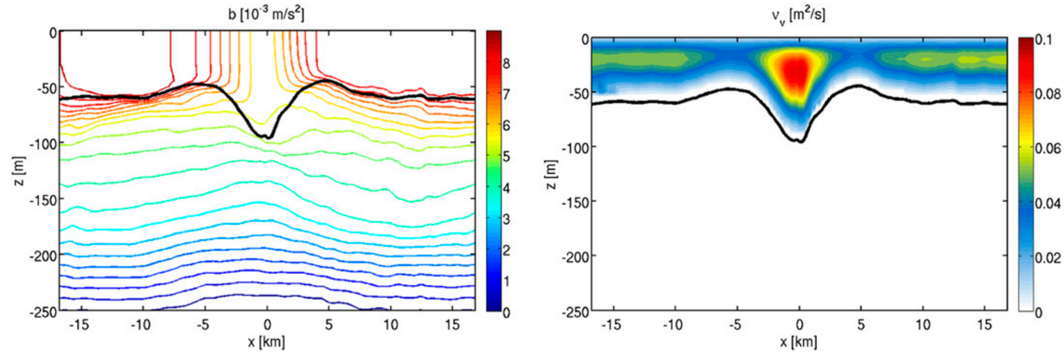

FIG. 2. Temporal snapshot of (left) $b(x, z)$ and (right) $\nu_\upsilon(x, z)$ for a filament in the Gulf Stream in a realistic ROMS simulation (Gula et al. 2014). These fields are averaged along the filament axis for a distance of 45 km. The black line denotes the boundary layer depth at $z = -h(x)$. Here, b has been detrended across the 34-km domain in x at each z.

2. Filament example in a realistic simulation

Computational simulations exhibit abundant populations of submesoscale surface fronts and filaments that arise in the presence of mesoscale eddies and boundary currents when the horizontal resolution is fine enough ($\Delta x \sim 1$ km; e.g., Capet et al. 2008a). To establish a context for the theoretical problem that follows, an example is taken from recent, realistic simulations of the Gulf Stream (Gula et al. 2014) made with the Regional Oceanic Modeling System (ROMS) (Shchepetkin and McWilliams 2005, 2008). Dense (cold) filaments frequently occur on the offshore edge of the stream. They have a typical life cycle of frontogenesis starting from mesoscale buoyancy gradients, barotropic instability, filament fragmentation, and filament disappearance, all occurring within an interval of about a day. The strong mean and mesoscale currents in the stream provide the strain for the filament frontogenesis.

An example taken at a time shortly before the onset of the barotropic instability is shown in Figs. 2–3. The first figure shows a transverse cross section of the buoyancy field $b(x, z)$ with some along-axis y averaging to smooth out various fluctuations, for example, internal waves. The b structure is a dense surface anomaly in the filament center within the well-mixed layer that weakens on the sides and down into the pycnocline. It has an associated boundary layer depth $h(x)$ that is deepest in the center, where the stratification is weakest, and decreases to the sides, with even a weak minimum depth (called a dimple) on the near edges of the filament. In the simulation model, h is determined independently within each vertical column as part of the K-profile parameterization (KPP; Large et al. 1994; McWilliams et al. 2009c) for the vertical eddy viscosity and diffusivity profiles $\nu_\upsilon(z)$ and $\kappa_\upsilon(z)$ within the surface turbulent boundary layer. The cross-sectional distribution of $\nu_\upsilon(x, z)$ closely

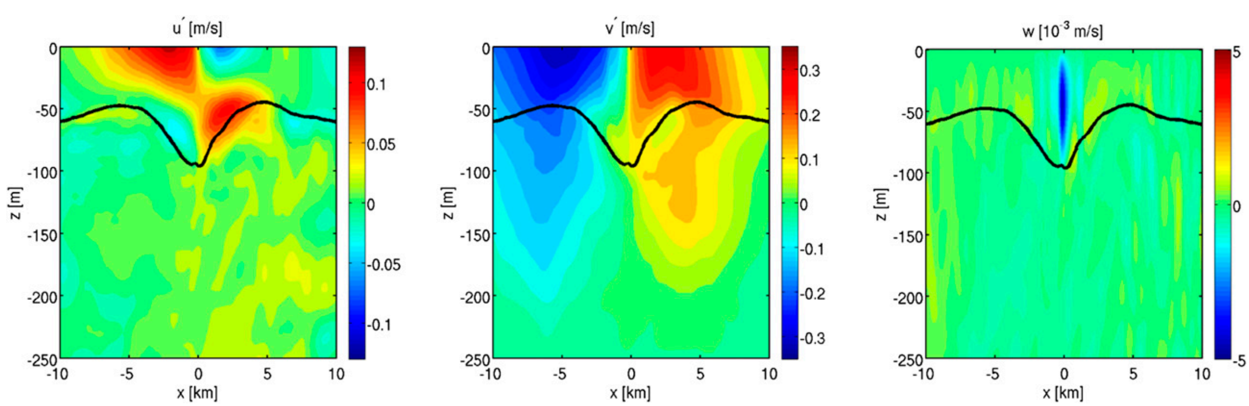

FIG. 3. Velocity fields (left) $u'(x, z)$, (middle) $\upsilon'(x, z)$, and (right) $w(x, z)$ for the same filament snapshot as in Fig. 2 (Gula et al. 2014). The black line denotes the boundary layer depth at $z = -h(x)$. The anomaly u' is relative to $z = -H$, and it has had its x mean (across the 34-km domain plotted in Fig. 2) removed at each height. The anomaly υ' is relative to $z = -H$, and it has had its geostrophic mean value removed at each height, that is, $\int_{-H}^{z} \langle \partial_x b \rangle \, dz/f$, where the angle brackets are an average in x and $\langle \partial_x b \rangle$ is the slope of the trend removed from b in Fig. 2.

follows that of h. This to be expected because, in KPP, ν_v is proportional to h times a turbulent velocity scale set by the surface momentum and buoyancy fluxes, and the surface fluxes have a larger horizontal (and temporal) scale of variation than does the filament itself. The field κ_v (not shown) has a similar structure. These fields are approximately even symmetric across the center.

The contemporaneous velocity field in Fig. 3 shows a double-jet structure in the longitudinal velocity $v(x, z)$, which is what is expected from geostrophic balance with $b(x, z)$. (Some removal of spatial means and trends is performed to bring out the local filament structure; this is described in the caption.) The secondary circulation in $u(x, z)$ and $w(x, z)$ is composed of two cells with surface inflow and horizontal convergence, central downwelling, outflow and divergence at depth, and weaker upwelling on the sides. This is the same pattern that is associated with strain-induced frontogenesis of a filament (McWilliams et al. 2009b), and some of it in the case here may be due to this cause. Nevertheless, as demonstrated in Gula et al. (2014), the primary horizontal momentum balance in this filament is among the Coriolis force, vertical momentum mixing, and the baroclinic pressure gradient force associated with the b anomaly, that is, not including the acceleration or the advection that, among its other effects, contains the mesoscale straining deformation. This type of approximate momentum balance is a combination of geostrophic and Ekman balances and is called the turbulent thermal wind (TTW; section 3). The maximum vertical vorticity (i.e., $\zeta \approx \partial_x v$ when the along-axis variations are small) normalized by f has a cyclonic value of 5.3 in the center of this filament example; that is, the local Rossby number Ro $= \zeta/f$ is large.

3. Turbulent thermal wind

Submesoscale flow structures are often identified by their $b(\mathbf{x})$ structure, in part because temperature measurements are among the most accessible, both on ships and from satellites. What kind of circulation inference can be made from b?

A quasi-steady linear momentum balance that combines hydrostatic, geostrophic, and Ekman boundary layer dynamics is called TTW [note that this term was introduced in Gula et al. (2014)]. For a horizontal shear vector $\mathbf{s}(z) = \partial_z \mathbf{u}_\perp(z)$ in the presence of a horizontal buoyancy-gradient profile $\nabla_\perp b(z)$ and sea level elevation η, with a vertical eddy viscosity profile $\nu_v(z)$ and a surface wind stress τ^s, the TTW problem is

$$f\hat{\mathbf{z}} \times \mathbf{s} = -\nabla_\perp b + \partial_z^2[\nu_v \mathbf{s}], \tag{1}$$

with boundary conditions

$$\begin{aligned} \nu_v \mathbf{s} &= \frac{\tau^s}{\rho_o} \quad \text{at} \quad z = \eta, \\ \mathbf{s} &\to \mathbf{s}_g \quad \text{as} \quad z \to -\infty, \end{aligned} \tag{2}$$

where the interior geostrophic shear profile is

$$\mathbf{s}_g(z) = \frac{1}{f}\hat{\mathbf{z}} \times \nabla_\perp b. \tag{3}$$

The subscript $\perp$ denotes a horizontal vector in the (x, y) plane. The vertical coordinate is z, and $\hat{\mathbf{z}}$ is the unit vertical vector. The associated TTW horizontal velocity is

$$\mathbf{u}_\perp(z) = \int_{zi}^{z} \mathbf{s}\, dz' + \mathbf{u}_{gi}, \tag{4}$$

and $\mathbf{u}_g$ is its geostrophic counterpart with $\mathbf{s}_g$. The ageostrophic TTW component

$$\mathbf{u}_a = \mathbf{u}_\perp - \mathbf{u}_g \tag{5}$$

contains the secondary circulation (u and w) for a 2D frontal or filamentary flow. By the second condition in (2), $\mathbf{u}_a$ vanishes going down into the interior. The depth z_i is an interior reference level where the geostrophic velocity is $\mathbf{u}_{gi}$. This TTW system is a 1D elliptical boundary-value problem in z, in which the (x, y, t) dependencies are parametric.

Given a 3D solution field for TTW $\mathbf{u}_\perp$, the continuity equation yields a TTW vertical velocity:

$$w = -\int_{z}^{\eta} \nabla_\perp \cdot \mathbf{u}_\perp \, dz', \tag{6}$$

assuming a rigid-lid approximation at the sea surface $w(\eta) = 0$. With an upper free surface, this w is augmented by the kinematic surface value $w(\eta) = [\partial_t + \mathbf{u}_\perp(\eta) \cdot \nabla_\perp]\eta$, which usually is small compared to the TTW interior w values from (6) for submesoscale filaments; for consistency of a single time diagnostic evaluation in TTW, the $\partial_t \eta$ term can be dropped in $w(\eta)$.

In the simple case of constant $\nabla_\perp b = \hat{\mathbf{x}} f S$ (S is the geostrophic shear), constant ν_{v0}, and zero surface wind stress (but finite ν_{v0} from whatever cause), the local TTW solution is

$$u = u_{gi} - \frac{h_e S}{2} e^{-z/h_e}\left[\cos\left(\frac{z}{h_e}\right) - \sin\left(\frac{z}{h_e}\right)\right]$$
$$v = v_{gi} + S(z - z_i) - \frac{h_e S}{2} e^{-z/h_e}\left[\cos\left(\frac{z}{h_e}\right) + \sin\left(\frac{z}{h_e}\right)\right], \tag{7}$$

where $h_e = \sqrt{2\nu_{v0}/f}$ is the usual Ekman depth scale, and, without loss of generality, η is here set to zero for this local column. (Because this model for $\mathbf{u}_\perp$ is linear, it can be superimposed with the usual wind-driven Ekman layer profile due to nonzero τ^s.) Thus, with $f > 0$ and northward geostrophic flow ($S, v_{gi} > 0$), the TTW ageostrophic flow is a counterclockwise Ekman spiral into the interior beneath a surface current with a magnitude $\sqrt{2}h_e S$ and directed toward the southwest (Fig. 4). By an integral of (7), the associated ageostrophic transport is equal to $h_e^2 S/2$ toward the south; that is, the longitudinal TTW flow is reduced compared to the geostrophic flow.

If there were neither turbulent mixing nor surface stress, then the filament would have a geostrophic along-axis flow and no secondary circulation. With a more realistic, convex, positive profile for $\nu_v(z)$ (e.g., from KPP; cf. Fig. 2), a $\mathbf{u}_\perp(z)$ profile occurs with roughly a similar shape to (7). With a surface wind stress τ^s, a classical Ekman layer profile can be superimposed on the buoyancy-gradient solution in Fig. 4. With horizontal variations in $\partial_x b$, ν_v, and τ^s, a vertical velocity will occur that is a baroclinic generalization of Ekman pumping. This is the basis for the 2D TTW secondary circulation in a filament (sections 4–5).

The approximate momentum-balanced model of Garrett and Loder (1981) is less complete than the TTW model through its neglect of the ageostrophic longitudinal flow. The model and its recent 3D extension in Ponte et al. (2013) are shown in Gula et al. (2014) to be less accurate than the TTW balance in finite-Ro circumstances, as in Figs. 2–3.

4. An idealized filament

a. *TTW implication for secondary circulation and frontogenesis*

As described in section 1, a surface filament has an upper-ocean strip of anomalous density compared to its horizontal environment in a stably stratified fluid. The associated geostrophic flow is thus a pair of surface-intensified jets on either side of the line. For a dense filament along a line parallel to $\hat{\mathbf{y}}$, the jet to the east is northward when $f > 0$, while the one to the west is southward (cf. v' in Fig. 3). The associated TTW ageostrophic flow (section 3) near the surface is thus directed to the southwest in the northward jet and to the northeast in the southward jet. This has the effect of reducing the total v in the jets and creating a convergent u toward the center of the filament, which will have a frontogenetic tendency by advection across the buoyancy gradients. This idea is developed more explicitly in the following subsections.

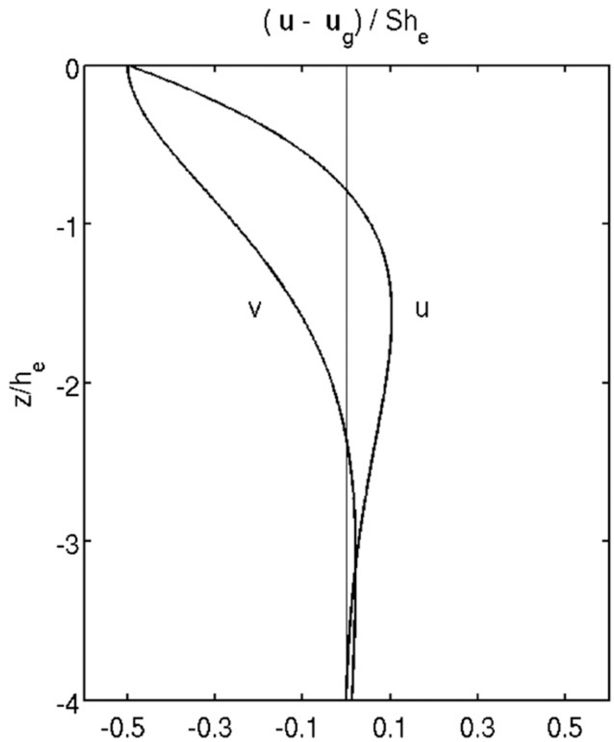

FIG. 4. Vertical profiles of ageostrophic TTW horizontal velocity $\mathbf{u}_a$ (i.e., relative to $\mathbf{u}_a = \mathbf{u} - \mathbf{u}_g$) for the simple case with depth-uniform $\partial_x b > 0$ and ν_{v0} and with zero surface wind stress.

In contrast, a light filament will have the reverse structure for its geostrophic jets. Thus, its TTW ageostrophic surface flow is toward the northeast in the southward jet to the east of the filament center and toward the southwest in the northward jet to the west of the center. This again implies a reduction in the total v, but now the cross-filament flow u is divergent away from the center, which will have a frontolytic tendency by its advection. For this reason, a light filament will tend to spread and weaken its flow under the influence of vertical momentum mixing. This is analogous to the secondary circulation of a light filament undergoing frontogenesis due to a background strain field, where the strain-induced secondary circulation has central upwelling and surface divergence; this opposes the direct frontogenetic tendency due to the strain flow's confluent advection, making the net rate of frontogenesis much weaker than for a dense filament (McWilliams et al. 2009b). Therefore, because light filaments are generally less intense than dense ones and are further weakened by the TTW effects of vertical mixing, no further consideration will be given to them in this paper.

b. Dense filament structure

An idealization of the filament structure, motivated by Fig. 2 and other examples, is the following: Assume there is a surface buoyancy profile $b_s(x)$ with a central minimum and a boundary layer depth $h(x)$ with a central maximum. The structure of $b(x, z)$ is divided into three layers. In the first layer, $b(x, z) = b_s(x)$ for $\eta(x) \geq z > -h(x)$; that is, the profile is well mixed. The third layer has uniform stratification, $b(x, z) = N_0^2(H + z)$ for $-H \leq z \leq -h_3 < -h(x)$, and it has no flow. The second layer is an interpolation between the first and third layers with continuous values and vertical derivatives at the interfaces and with its density stratification concentrated just below the boundary layer:

$$b(x,z) = [b_s(x) - b_3]F(\xi) + b_3, \quad \xi = \frac{-z - h(x)}{h_3 - h(x)},$$
$$F(\xi) = \frac{e^{a(1-\xi^\mu)} - 1}{e^a - 1}, \tag{8}$$

where $b_3 = b(-h_3) = N_0^2(H - h_3)$, and $a(x)$ satisfies the derivative continuity condition at the bottom of the second layer

$$\frac{\mu a}{e^a - 1} = N_0^2 \frac{h_3 - h(x)}{b_s(x) - b_3} > 0. \tag{9}$$

The parameter $N_0^2 > 0$ is the deep stratification. The parameter $\mu > 1$ regulates how strongly the pycnocline is concentrated just below the boundary layer (i.e., more so for smaller $\mu > 1$). This profile has $\partial_z b \geq 0$ everywhere and is monotonic below $z = -h(x)$.

The idealized form for the vertical eddy viscosity, chosen here partly independent from $b(x, z)$ and the surface flux (note that their mutual consistency is enforced in section 5a), is the following:

$$\nu_v(x,z) = \nu_{v0} G(\lambda) \frac{h(x)}{h_0} + \nu_{vb}, \quad \lambda = -\frac{z}{h},$$
$$G(\lambda) = C_G(\lambda_0 + \lambda)(1 - \lambda)^2, \quad \lambda \leq 1,$$
$$= 0, \qquad \lambda \geq 1. \tag{10}$$

The parameter h_0 is the far-field boundary layer depth. The parameter $0 < \lambda_0 \ll 1$ is a small regularization constant to avoid a logarithmic singularity in $\mathbf{u}_\perp$ as $z \to 0$. The parameter $0 < \nu_{vb} \ll \nu_{v0}$ provides a small background diffusivity in the interior. The relation $C_G = 4(1 + \lambda_0^2)/27$ makes the vertical column maximum of $G = 1$. This is a simplified $\nu_v(x, z)$ shape approximately as assumed in the KPP scheme (Large et al. 1994), consistent with a uniform turbulent velocity scale (related to the surface momentum and buoyancy fluxes but here represented by ν_{v0}/h_0), a convex vertical profile shape within the boundary layer, and a column peak magnitude proportional to $h(x)$. (See section 5 for the actual KPP solutions.)

These functions are evaluated for profiles that express a central minimum in $b_s(x)$ and maximum in $h(x)$ appropriate to a cold/dense filament core:

$$b_s(x) = b_{s0} - \delta b_0 \exp[-(x/L)^2],$$
$$h(x) = h_0 + \delta h_0 \exp[-(x/L)^2]. \tag{11}$$

No attempt is made to closely match the numerical values in Fig. 2, which are a result of a complex and imprecisely known evolutionary process within the realistic simulation (Gula et al. 2014). Rather, plausibly similar values are chosen for illustrative purposes with similar deep stratification and somewhat weaker filament and boundary layer mixing strengths, namely,

$$H = 250\,\mathrm{m}, \quad N_0^2 = 3.44 \times 10^{-5}\,\mathrm{s}^{-2},$$
$$f = 7.81 \times 10^{-5}\,\mathrm{s}^{-1}, \quad h_3 = 130\,\mathrm{m},$$
$$b_3 = 4.13 \times 10^{-3}\,\mathrm{m\,s}^{-2}, \quad b_{s0} = 8.51 \times 10^{-3}\,\mathrm{m\,s}^{-2},$$
$$\delta b_0 = 1.43 \times 10^{-3}\,\mathrm{m\,s}^{-2}, L = 3.5\,\mathrm{km}, \quad h_0 = 60\,\mathrm{m},$$
$$\delta h_0 = 17\,\mathrm{m}, \quad \mu = 1.1, \quad \lambda_0 = 5.0 \times 10^{-3},$$
$$\nu_{v0} = 3.86 \times 10^{-2}\,\mathrm{m}^2\,\mathrm{s}^{-1}, \quad \nu_{vb} = 1.0 \times 10^{-4}\,\mathrm{m}^2\,\mathrm{s}^{-1}. \tag{12}$$

The resulting fields are calculated by solving the TTW vertical boundary-value problem independently at each x as described in the appendix, and they are shown in Fig. 5. The velocities satisfy the TTW equations with no surface wind stress at each horizontal location. (The consistent inclusion of τ^s and ν_v is done in section 5a.) Because $\partial_x b < 0$ on the west side, the ageostrophic TTW $u > 0$, and vice versa, on the east side. Thus, the TTW circulation for a filament has surface horizontal convergence and central downwelling. This circulation pattern is qualitatively similar to that in Fig. 3, but here without any wind-driven Ekman currents. In particular, this shows that the double-celled secondary circulation can be entirely due to $\nu_v(x, z)$ in the presence of $b(x, z)$ as a TTW circulation, and its structural similarity to the strain-induced frontogenetic secondary circulation

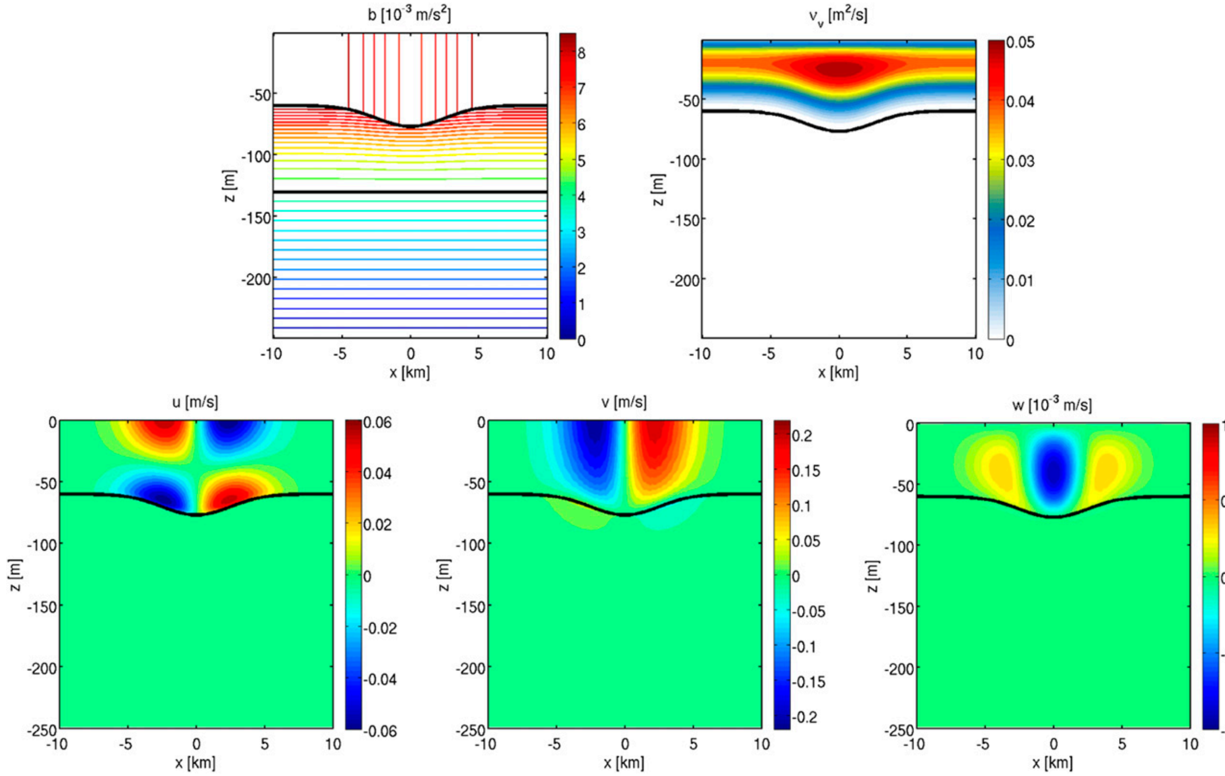

FIG. 5. (top, left) Buoyancy, (top, right) vertical eddy viscosity, and (bottom) TTW velocity fields for an idealized filament with the parameters in (12). The black lines denote the boundary layer depth at $z = -h(x)$ or (for buoyancy) $z = -h_3$.

(Fig. 1; McWilliams et al. 2009b) means that detection of this flow pattern alone is insufficient to distinguish between these two processes to infer the evolutionary dynamics of a filament. Note also that the secondary circulation implies a net conversion of potential to kinetic energy $\iint wb\,dx\,dz > 0$ in both situations.

In contrast to the solution in (7) with constant ν_v and constant $\partial_x b$, the parameter dependencies of the TTW circulation for this $\nu_v(x, z)$ and $b(x, z)$ problem are somewhat complex; for example, by simply varying ν_{v0} with the other parameters in (12) held fixed, the central downwelling is strongest for $\nu_{v0} \approx 7.5 \times 10^{-2}\,\mathrm{m^2\,s^{-1}}$ with $\min(w) \approx -0.93 \times 10^{-3}\,\mathrm{m\,s^{-1}}$ (i.e., only slightly larger than in Fig. 5, lower right). The ν_{v0} dependencies are nonmonotonic because the shape of the secondary circulation changes somewhat with this parameter. Overall, the variations in (u, w) are not strong functions of the eddy viscosity parameters. The reason is that the $z = 0$ boundary condition in (2) with $\tau^s = 0$ is $\partial_z \mathbf{u}_a = -\mathbf{s}_g$, independent of the value of ν_v, and this is the only forcing term for the ageostrophic horizontal TTW circulation. In section 3, the eddy viscosity only matters in determining the Ekman boundary layer depth scale $h_e \propto \sqrt{\nu_{v0}}$, which here is controlled by $h(x)$ in (11), and the strength of the ageostrophic secondary circulation is Sh_e in (7). Thus, the stronger the surface geostrophic shear and the deeper the boundary layer depth (or stronger the turbulent mixing), the stronger is the TTW ageostrophic secondary circulation. When $\nu_v(x, z)$, as in (10), this will cause additional spatial variation in $\mathbf{u}_a$ and especially in w from (6); however, because the mixing coefficient dependencies are fairly weak and the TTW system is readily calculable, the full parameter dependencies are not mapped.

Notice that this $h(x)$ profile does not have a dimple on the filament edges, and hence ν_v does not have a minimum there. This choice is made mainly for simplicity; the possibility of an evolutionary development of a dimple is discussed in section 5b.

c. Frontal tendency

A diagnostic Lagrangian frontal tendency balance relation can be formulated for the horizontal gradient variances, as has often been done for $(\partial_x b)^2$ for buoyancy fronts (Hoskins 1982; Capet et al. 2008b). With the different shape of a buoyancy filament (and anticipating the frontogenetic evolution in section 5),

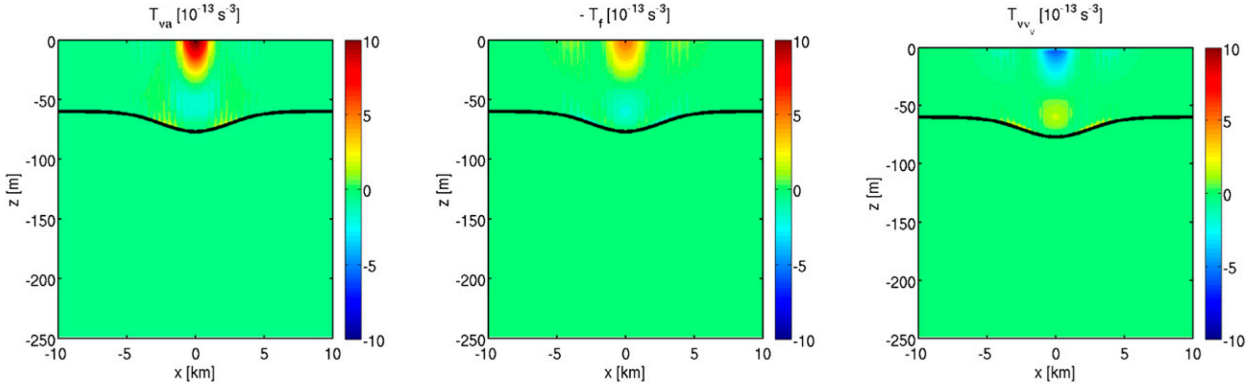

FIG. 6. Frontal tendency terms in the $(\partial_x v)^2$ balance [(13)]: (left) advection, (middle) Coriolis conversion, and (right) vertical mixing. These are evaluated for the idealized TTW filament in Fig. 5. The black line denotes the boundary layer depth at $z = -h(x)$.

this balance is a more informative diagnostic for $(\partial_x v)^2$, namely, for a 2D solution:

$$
\begin{aligned}
\frac{D}{Dt}\frac{1}{2}(\partial_x v)^2 &= T_{va} - T_f + T_{vv_v} + T_{vv_\perp} \\
T_{va} &= -\partial_x v(\partial_x u \partial_x v + \partial_x w \partial_z v) \\
T_f &= f\partial_x u \partial_x v \\
T_{vv_v} &= \partial_x v \partial_x \partial_z(\nu_v \partial_z v) \\
T_{vv_\perp} &= \nu_\perp \partial_x v \partial_x^3 v. \qquad (13)
\end{aligned}
$$

The right-side tendency terms are, respectively, advection by the secondary circulation, exchange with the analogous balance relation for $(\partial_x u)^2$ through the Coriolis force, and vertical and horizontal eddy viscous diffusion (assuming a constant $\nu_\perp$). Even though the focus here is on $(\partial_x v)^2$, rather than $(\partial_x b)^2$ and $(\partial_x u)^2$, the presumption is that they all will grow together in a frontogenetic event if a degree of continuing adjustment toward TTW balance is maintained during the evolution; this is assessed in section 5b.

Figure 6 shows the primary tendency terms. The secondary circulation advection in T_{va} is dominant, and it is frontogenetic in the upper center in the sense of increasing $\partial_x v > 0$ and hence also cyclonic ζ, thus narrowing the horizontal distance between the two longitudinal velocity jets. The Coriolis tendency T_f is similarly frontogenetic with about half the magnitude of T_{va}. It represents an exchange with the Lagrangian tendency balance for $(\partial_x u)^2$ where it appears with an opposite sign. The vertical mixing tendency T_{vv_v} has nearly the same magnitude as T_f but has the opposite sign; hence, it is frontolytic, as might intuitively be expected for a mixing process. The horizontal mixing tendency $T_{vv_\perp}$ is about two orders of magnitude weaker with a $\nu_\perp$ value of 0.1 $m^2 s^{-1}$ (section 5), and its pattern is mostly negative (frontolytic), as expected. The net of these tendency terms, however, is strongly frontogenetic. This raises the question of how a TTW filament will evolve, which is addressed in the next section.

5. Evolution of an idealized dense filament

a. Setup and initial condition

The preceding idealized filament is ad hoc in the sense that $b(x, z)$ and $\nu_v(x, z)$ are independently chosen for determining $\mathbf{u}$ by the TTW relations. A more consistent alternative is to specify all of these fields together with a boundary layer parameterization scheme, which is chosen as KPP, consistent with the simulation results in Figs. 2–3. This means that the mixing coefficients ν_v and κ_v will be consistent with b and $\mathbf{u}$ as well as with the surface boundary forcing that sustains the boundary layer turbulence. For simplicity, choose a wind-driven case without surface buoyancy flux, for example, with constant eastward wind stress

$$\boldsymbol{\tau}^s = \tau_0 \hat{\mathbf{x}} \qquad (14)$$

and $\tau_0 = 0.1\ \mathrm{N\,m^{-2}}$. The qualitative behavior of the filament evolution is not strongly dependent on wind direction [in contrast to the centrifugal instability instigation mechanism of Thomas and Lee (2005)]. With a nonzero surface stress, there will be a wind-driven (i.e., Ekman layer) component to the TTW solution superimposed with the $\partial_x b$ component. There is a bulk advective movement of the filament by the Ekman circulation (or any other ambient larger-scale circulation), which is least in the direction perpendicular to the Ekman transport, that is, trivially to the south for (14). (ROMS solutions with different wind directions have been obtained but for brevity are not shown.)

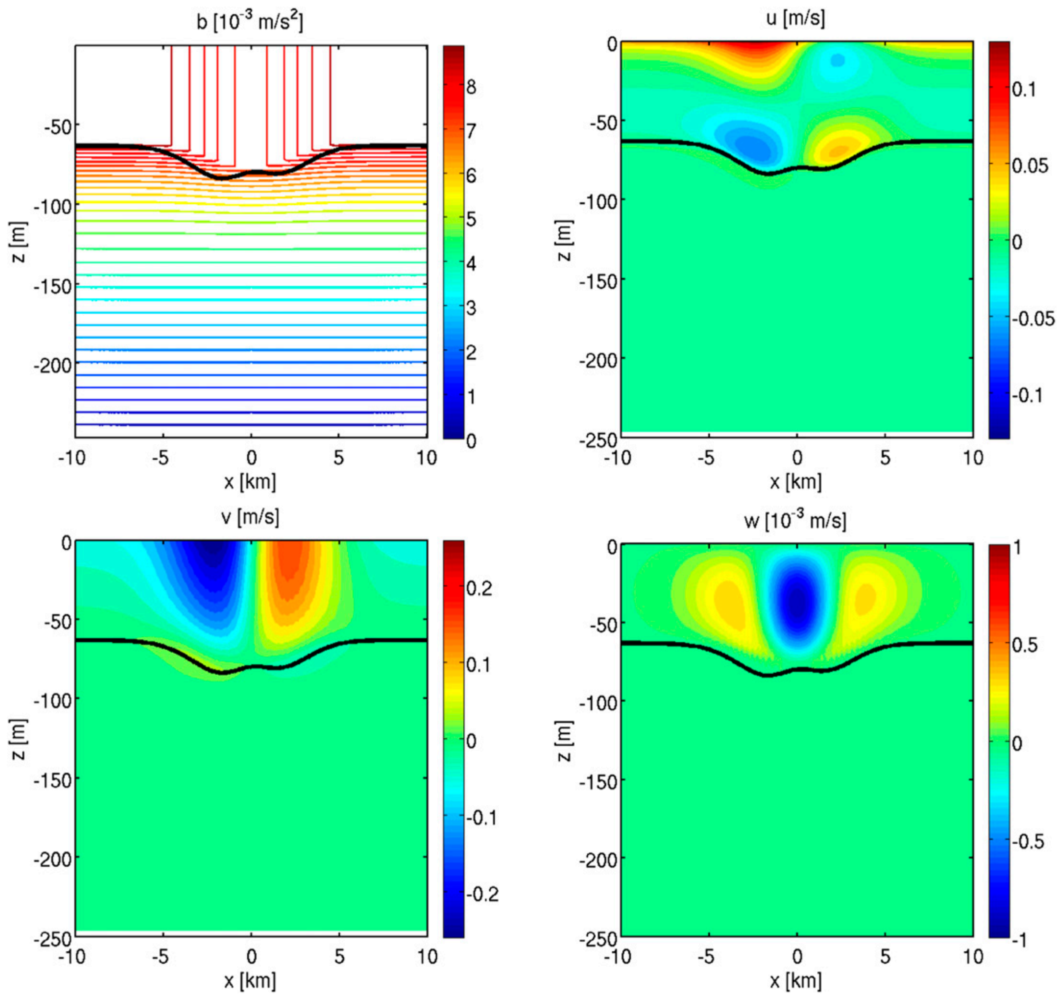

FIG. 7. Buoyancy and TTW velocity fields for an idealized filament with the same b as in Fig. 5 and the KPP-consistent eddy viscosity shown in Fig. 8 with the wind stress in (14). The color bar ranges are the same as in Fig. 5 for b and w but are somewhat larger for u and v. The black line denotes the boundary layer depth at $z = -h(x)$. The turbulent entrainment velocity here is $V_0 = 0.15\,\mathrm{m\,s^{-1}}$. This is the initial condition for the ROMS integration.

To make the initial condition compatible with ROMS using KPP and TTW, the following iterative procedure is followed:

(i) Specify $b(x, z)$ by (8), $\eta(x)$ by hydrostatic integration from flat pressure surfaces at depth, $\tau^s(x)$ by (14), and a first guess for $\nu_v^0(x, z)$ by (10).
(ii) Set the iteration count to $n = 0$.
(iii) Calculate $\mathbf{u}^n(x, z)$ by the TTW relations in the appendix from b, η, τ^s, and ν_v^n.
(iv) Calculate $\nu_v^{n+1}(x, z)$ by the KPP model using b, τ^s, and $\mathbf{u}^n$.
(v) Set $n = n + 1$ and iterate steps iii–iv until convergence.
(vi) Determine $\kappa_v(x, z)$ by KPP from the final b, τ^s, and $\mathbf{u}$.

The result will have the same b as in Fig. 5a but a different $h(x)$ as well as a different ν_v and $\mathbf{u}$. In this wind-driven case without surface buoyancy flux, $\kappa_v = \nu_v$. Finally, the sea level height $\eta(x)$ is determined by hydrostatic integration upward from deep in the interior where the horizontal pressure gradient vanishes; for the dense/cold filament, η has a weak central depression of about 0.01 m relative to the exterior.

The consistent filament initial condition is shown in Figs. 7–8. There are strong similarities to the idealized filament fields in Fig. 5. The largest differences are due to the wind-driven flow, which is dominant in the far-field profile (Fig. 8b) but, of course, present throughout the domain. Its velocities are relatively weak compared to those in the filament. It does break the x symmetry in the filament to a moderate degree, as seen in u, v, h, and ν_v. It also breaks the superposition of wind and baroclinic components of the TTW velocity because the

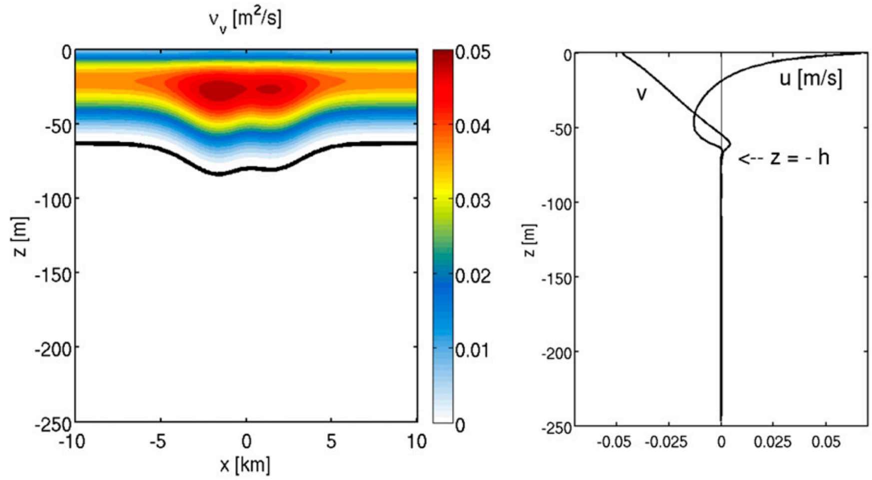

FIG. 8. (left) Eddy viscosity and the (right) Ekman layer velocity profile in the far field, which would be zero with no wind stress. These are for the KPP-consistent initial conditions and accompany the b and $\mathbf{u}$ fields in Fig. 7. The turbulent entrainment velocity here is $V_0 = 0.15\,\mathrm{m\,s^{-1}}$.

consistent $\nu_v(x, z)$ is a nonlinear function of both components. Comparing the ν fields in Figs. 5 and 8, left panel, the x asymmetry in the latter arises because of the asymmetry of the superimposed Ekman and geostrophic velocity fields. The vertical velocity is unaffected by τ^s directly because of its spatial uniformity, but it is modestly influenced by the horizontally variable Ekman current associated with variable $\nu_v(x, z)$. The frontal tendencies (13) evaluated for the consistent initial condition (not shown) are similar to those in Fig. 6, again with the implication of a frontogenetic tendency in $(\partial_x v)^2$ at the core of the filament.

A ROMS integration is performed with this idealized filament initial condition. The 2D integration domain is $L \times H$ with $L = 20\,\mathrm{km}$ and $H = 250\,\mathrm{m}$. The grid size is $N_x \times N_z$, with $N_x = 1600$ ($\Delta x = 12.5\,\mathrm{m}$) and $N_z = 640$ in the highest-resolution cases. Over a range of grid sizes down to 10 times smaller than these N_x and N_z values, there are no important qualitative differences in the solution behavior, although there are moderate quantitative differences (e.g., in the peak vorticity; Fig. 11). The horizontal boundary condition is periodicity. The top is a free surface with the wind stress (14) and no buoyancy flux. The bottom boundary conditions are $w = 0$ and zero stress.

The boundary layer vertical mixing parameterization scheme is the single-column, single-time KPP whose equations are presented in Large et al. (1994), and ROMS uses the alternative prescription for determining the boundary layer depth h in the appendix of McWilliams et al. (2009c). Its physical rules were devised for horizontally homogeneous, temporally stationary, or self-similarly developing (e.g., penetrative convection) circumstances. In large-scale circulation models, where KPP is widely used, these assumptions are a plausible characterization of the boundary layer environment.

In this filament problem, with its strong lateral gradients and rapid time development, however, KPP is being applied well beyond its realm of calibration and validation *faute de mieux*; that is, the same caveat could be stated about all other extant subgrid-scale mixing parameterizations in an active submesoscale regime. The conceptual fallacy is taking an overly local view of the turbulent mixing, that is, ignoring (x, y, t) connectivity in KPP or even (x, y, z, t) connectivity in single-point second-moment closures such as k–ϵ (Davidson 2004).

In performing the ROMS integrations, it was discovered that fine structure often develops on the sides of the filament in the KPP-diagnosed $h(x, t)$ and hence appears in $\nu_v(x, z, t)$ and $\kappa_v(x, z, t)$. Its signature is local, sudden but time reversible, increases in h by about 10–20 m in the regions underneath the strongest surface horizontal buoyancy gradients where, as will be shown, h generally retreats with time, and the residual vertical stratification underneath becomes very weak, partly because of lateral advection of filament-core water by the divergent circulation at depth under the flanks of the filament. These jumps happen rarely and at essentially separate x and t points, but nevertheless they are implausible as a representation of ensemble-mean turbulence that should vary smoothly in space and time on the scale of its environment.

The formulation used for determining h in KPP is the alternative integral condition in McWilliams et al. (2009c) instead of the original bulk Richardson number condition in Large et al. (1994). Both include a turbulent velocity scale V_t, which was originally proposed to represent entrainment by convective plumes by deepening h to reach into the stable stratification at the base of the mixed layer (i.e., the ''inversion'' layer), and it has recently been proposed to additionally represent entrainment by Langmuir circulations in the presence of surface gravity waves (McWilliams et al. 2014). To ameliorate the fine structure, the V_t term is further incremented by a constant velocity scale V_0, with both the a posteriori rationale of smoother solutions and an a priori rationale of additional turbulent generation by the filament profiles. Values for V_0 are chosen between 0 and $0.15\,\mathrm{m\,s^{-1}}$, that is, about the same size as the filament horizontal velocities in Fig. 7; much larger values would be inappropriate by causing excessive boundary layer deepening. Even more powerful in ensuring the smoothness of $h(x, t)$ is the use of a limiter for its local rate of change

$$\left|\frac{\partial h}{\partial t}\right| \le \frac{h}{t_*} \to |h(x, t+\Delta t) - h(x, t)| \le \frac{\Delta t}{t_*} h(x, t) \qquad (15)$$

at every x, where Δt is the model time step size (i.e., 12 s on the finest spatial grid), and t_* is an adjustment time to achieve a new turbulent equilibrium in the boundary layer. That is, at the new time the KPP prescription for $h(x, t+\Delta t)$ is limited in how much it can change from the prior time $h(x, t)$ to not exceed this right-side limiter. Rough estimates of t_* are an Ekman response time $f^{-1} \approx 1.4 \times 10^4$ s or a vertical velocity eddy turnover time $h/w \approx 7.0 \times 10^4$ s. An appreciable smoothing benefit in $h(x, t)$ is evident for $t_* \ge 10^4$ s, and the solutions in section 5b are for $t_* = 4.0 \times 10^4$ s whose $h(x, t)$ solutions are quite smooth in time. Of course, these incremental KPP specifications of V_0 and t_* are quantitatively ad hoc and chosen to assure that the boundary layer mixing behaves similarly to that seen in full ROMS simulations with the native KPP (section 2). These issues are further discussed in sections 5b and 7.

An explicit horizontal eddy viscosity and diffusivity have sometimes been included in exploratory solutions, with the largest values of $\nu_\perp = \kappa_\perp = 0.5\,\mathrm{m^2\,s^{-1}}$, which is up to 10 times larger than the peak value in the initial ν_v (Fig. 8). However, the results in the following four plots are for $\nu_\perp = \kappa_\perp = 0$. The ROMS horizontal advection operator is third-order upstream biased, and hence it implicitly has a flow-adaptive hyperdiffusive effect near the grid scale independent of any explicit diffusivity. None of these horizontal diffusive effects are of any consequence until the late stage of filament frontogenesis after the central velocity gradient scale has approached the horizontal grid scale (section 5b). We only briefly consider the later stages after a diffusive arrest of the frontogenesis (see Fig. 13 and the associated discussion); no particular physical credence is to be given to the horizontal eddy diffusivities that represent the small-scale turbulence that causes the arrest until a more fully 3D simulation can discover what their proper cause might be.

b. Frontogenetic evolution

The filament evolution proceeds from the initial fields in Fig. 7 to those at $t = 0.65$ days in Fig. 9. Overall, the spatial configurations are preserved, but many aspects have changed. Most strikingly, the distance between the two longitudinal v jets has shrunk, as has the width of the central w downwelling. The frontal structure in b, v, and w is rather deep, extending most of the way through the boundary layer. The field $\zeta(x, z)$ (not shown) also exhibits a narrow, deeply extended extremum. The horizontal scale over which $u(x, \eta)$ reverses sign has similarly shrunk. These are manifestations of frontogenesis. The buoyancy b has developed a kink at the surface, and its isolines have tilted within the mixed layer, consistent with the surface convergence and subsurface divergence in the secondary circulation. The function $h(x)$ has diminished in magnitude, and the width of its central region of deep values has shrunk. In the locations where h has shrunk the most (even to the point of developing a dimpled shape), fine structure fluctuations in $h(x, t)$ can arise on the lower side of the filament—in the absence of the time-limiter condition (15)—in which neighboring points can jump between the mostly diminished values and the deeper original values; it is clear from $b(x, z)$ that this vertical interval is one of very weak or even slightly unstable stratification between a weak pycnocline above and the main pycnocline below. There are faint indications of internal gravity waves in the pycnocline in the interior colorations in u and w and small undulations in the b contours; their presumptive source is the rapid time development of the filament that exhibit a degree of momentum imbalance relative to the TTW approximation (see the discussion of $\mathcal{R}$ near the end of this section).

By this time of $t = 0.65$ days, the fields in the filament center have reached a limit of effective resolution with <10 grid points in the central extrema in w and $\zeta = \partial_x v$. Afterward the model integration proceeds without blowup, but there is no further sharpening of the central gradients, and the magnitudes of these extrema begin to decay. The time of this grid-scale limitation is remarkably insensitive to the parameter choices for N_x, N_z, V_0, ν_{vb}, κ_{vb}, and $\nu_\perp = \kappa_\perp$, consistent with the interpretation of a conservative evolution approximately

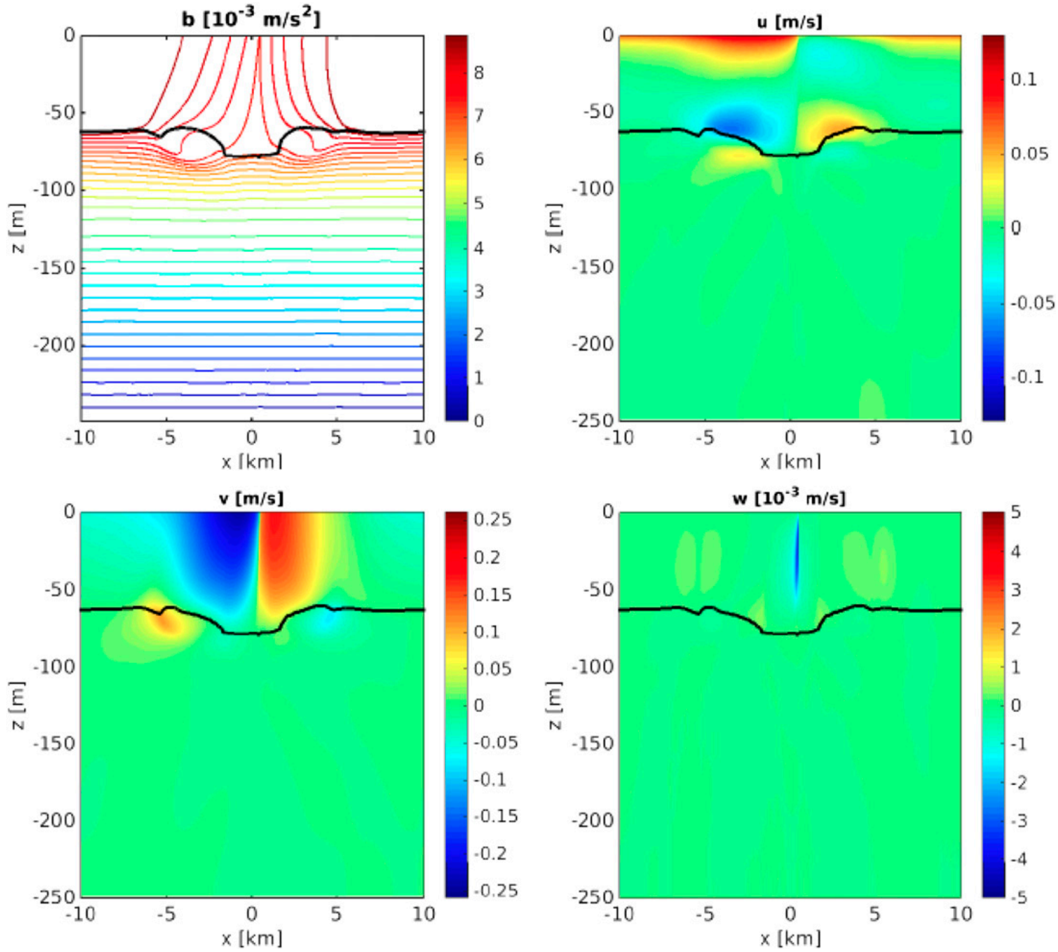

FIG. 9. Buoyancy and velocity fields at $t = 0.65$ days in the ROMS integration with the $t = 0$ initial condition in Fig. 7; the contour and color ranges are the same as at $t = 0$ except for a larger range for w. The black line denotes the boundary layer depth at $z = -h(x)$. This case has $V_0 = 0.15\,\mathrm{m\,s^{-1}}$ and $\nu_\perp = \kappa_\perp = 0$.

toward a finite-time singularity (section 6), which would imply a very steep cost–benefit curve for increasing resolution around this time. The insensitivity of this time to $\nu_\perp = \kappa_\perp$ within the range of values explored indicates that the model's implicit hyperdiffusion is playing an important role in limiting the frontogenesis. Consistent with this, the peak magnitudes of, for example, w and ζ, do increase with the grid numbers and decrease with the explicit horizontal diffusivities. Because the model solution is computationally unreliable once the grid-scale limitation is reached, no further attention will be given to later times. With larger $\nu_\perp$ and $\kappa_\perp$, no doubt a quasi-steady state arrest could be achieved, but this is not of great interest in the absence of a dynamical explanation for these elevated diffusivity values.

A more detailed view of the horizontal structure at the surface is in Fig. 10, comparing profiles at $t = 0$ and 0.65 days for b, u, and v. The b profile becomes more nearly linear on both sides of the filament and closely approximates a cusp at the center. There is a general increase with time indicating convergent advection toward the center. The central magnitude itself increases only slightly, perhaps due to horizontal diffusion, and it moves <1 km to the east because of the eastward surface Ekman velocity (Fig. 8, left panel). The u and v profiles both manifest a near discontinuity at the center of the filament because of the advective convergence in the secondary circulation; this near discontinuity is the emergent frontal structure of a filament under the influence of boundary layer mixing. All three profiles exhibit vanishing temporal changes in the far field.

Time series of the central downwelling w and central cyclonic vorticity ζ are shown in Fig. 11. Except for a very early adjustment in w, both series show monotonic growth for the plotted time interval. The final time of $t =$ 0.65 days is close to the largest extremum in w as the limit of grid resolution is approached, although the ζ extremum continues to increase up until about $t = 0.8$ days (not

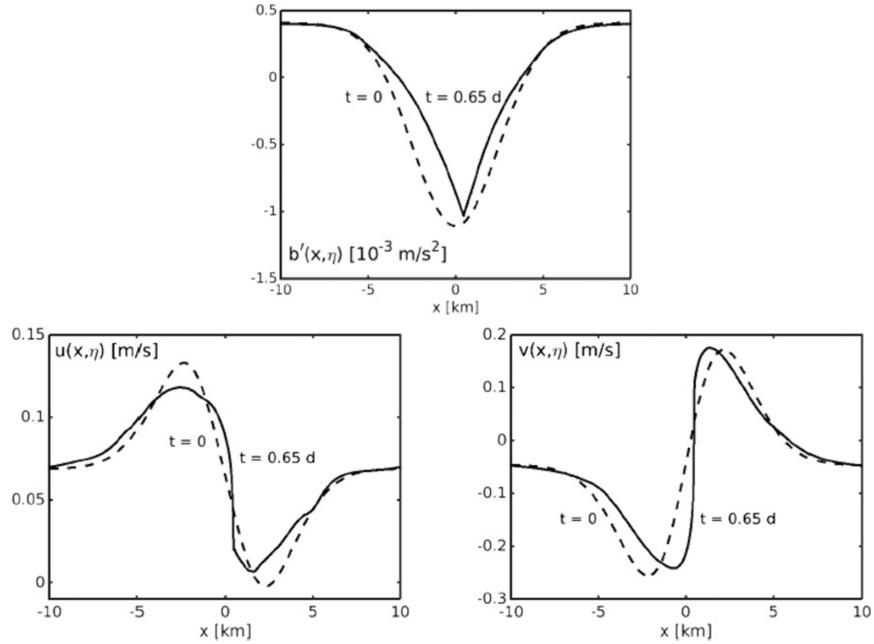

FIG. 10. Cross-filament profiles in the ROMS integration at the surface for $b'(x, \eta)$ (i.e., with horizontal average subtracted), $u(x, \eta)$, and $v(x, \eta)$ at $t = 0$ (dashed lines) and $t = 0.65$ days (solid lines), which is the time of maximum downwelling at the filament center (Fig. 11).

shown). The largest w value is $0.5\,\mathrm{cm\,s^{-1}}$, which is quite large for oceanic mesoscale and submesoscale currents with approximate momentum-balanced dynamics. The largest ζ value of $4.6 \times 10^{-3}\,\mathrm{s^{-1}} = 58f$ means that the local Rossby number becomes very large.

Parameter sensitivities for this solution are previously discussed where the values of N_x, N_z, V_0, $\nu_\perp$, and $\kappa_\perp$ are given. None of them qualitatively changes the frontogenetic evolution at the filament center. Even when $V_0 = t_* = 0$ is chosen in KPP and $h(x, t)$ fine structure arises (section 5a), this does not influence the primary flow evolution, although it does act as a weak source of internal gravity wave excitation and propagation downward into the interior. Furthermore, an extreme choice of holding $\nu_\upsilon(x, z)$ and $\kappa_\upsilon(x, z)$ fixed in time at their initial values still supports filament frontogenesis at approximately the same rate as seen with consistent interactive boundary layer mixing, albeit with peculiar behavior near the bottom of the layer; that is, the existence of the secondary circulation is due more to the existence of vertical momentum mixing in the boundary layer than it is to its particular strength or structure.

The smoothly evolving boundary layer depth $h(x, t)$ with $t_* \neq 0$ is moderately dependent on the value of the turbulent entrainment velocity V_0, as illustrated in Fig. 12, that compares h for cases with $V_0 = 0.1$ and $0.15\,\mathrm{m\,s^{-1}}$. The function h is smaller with the smaller V_0, as expected because the entrainment velocity is smaller. The function h generally decreases with time due to the rearrangement of the b and $\mathbf{u}$ fields by increased density stratification associated with lateral advection of dense water away from the filament center near the bottom of

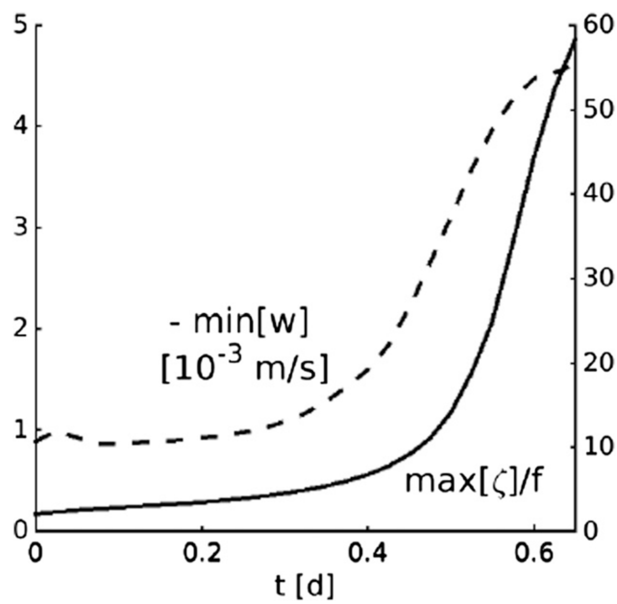

FIG. 11. Time series of spatial extrema in w (left ordinate) and ζ/f (right ordinate) in the ROMS integration up to the time of the largest central downwelling value ($t = 0.65$ days). The latter is a peak local Rossby number. The horizontal eddy diffusivities are zero here.

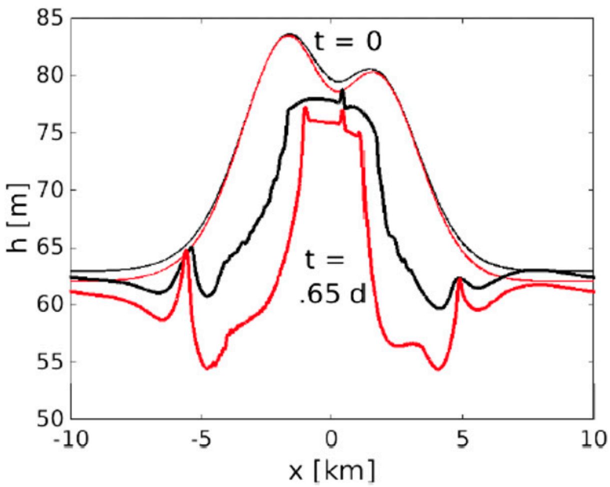

FIG. 12. Boundary layer depth $h(x)$ for two ROMS integrations with different V_0 values in KPP. Dashed lines are for $t = 0$ and solid lines are for $t = 0.65$ days; black lines are for $V_0 = 0.15\,\mathrm{m\,s^{-1}}$, and red lines are for $V_0 = 0.10\,\mathrm{m\,s^{-1}}$. The function $h(x, t)$ mostly increases with V_0. Here, $\nu_\perp = \kappa_\perp = 0\,\mathrm{m^2\,s^{-1}}$.

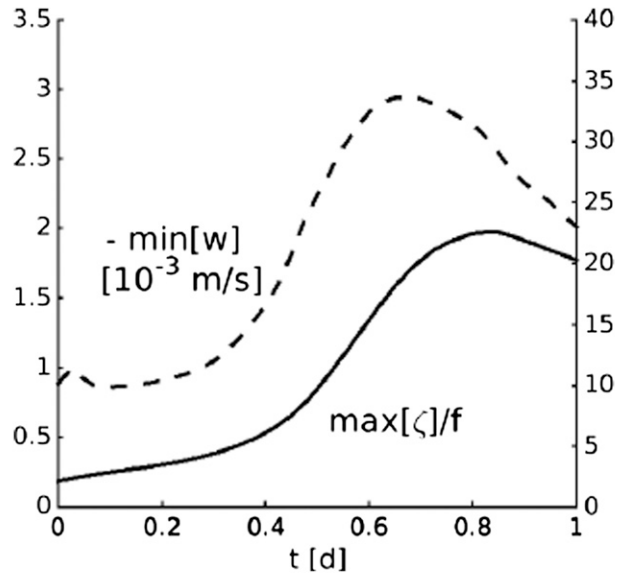

FIG. 13. As in Fig. 11, but with $\nu_\perp = \kappa_\perp = 0.5\,\mathrm{m^2\,s^{-1}}$. Notice the reduction of the ordinate range and the extension of the time period displayed.

the boundary layer. Interestingly, the smaller $h(x)$ values on the filament sides show the development of a dimple in h, where h is less than it is in the far field, with the smaller value of $V_0 = 0.1\,\mathrm{m\,s^{-1}}$; this tendency is even stronger with smaller V_0. This behavior echoes the dimple in the realistic simulation example in Fig. 2. The explanation is that the divergent branch of the secondary circulation in the lower part of the boundary layer advects central dense water underneath the lighter surface water on the filament edge, while the convergent surface circulation advects lighter water from the sides. These tendencies increase the vertical buoyancy stratification, which inhibits boundary layer penetration. This process occurs in competition with the boundary layer deepening by entrainment mixing. The outcome is dependent upon the entrainment velocity V_0. At the present level of uncertainty about how to parameterize the boundary layer turbulence in an evolving submesoscale filament, no strong conclusion should be drawn about when dimples will develop.

The influence of horizontal eddy diffusion is explored in an alternative ROMS simulation with $\nu_\perp = \kappa_\perp = 0.5\,\mathrm{m^2\,s^{-1}}$ (Fig. 13). The progression toward frontogenesis proceeds much as in the previous solution, and the peak values of w and ζ are reached at almost the same times, albeit with reduced magnitudes. The effect of this added mixing is to arrest the frontogenesis on a finite scale that is well resolved on the model grid. In the later stages following the arrest, the filament enters a period of slow decay as the central buoyancy anomaly and its associated TTW circulation are eroded by the lateral mixing.

The initial conditions, by construction, satisfy exactly the TTW balance with the KPP-consistent vertical viscosity (section 5a). How well is this balance maintained during the subsequent evolution? This is assessed by diagnostically calculating $\mathbf{u}_\perp^{\mathrm{TTW}}$ from (1) to (2) given the b, ν_υ, κ_υ, and τ^s fields as they occur at each time in the ROMS integration with $V_0 = 0.15\,\mathrm{m\,s^{-1}}$ and $\nu_\perp = \kappa_\perp = 0\,\mathrm{m^2\,s^{-1}}$. The fractional departure from TTW balance is measured by

$$\mathcal{R}(t) = \frac{\mathrm{rms}[\mathbf{u}_\perp^{\mathrm{TTW}} - \mathbf{u}_\perp]}{\mathrm{rms}[\mathbf{u}_\perp]}, \qquad (16)$$

where rms[ ] denotes the total root-mean-square variation of the vector velocity within a (x, z) spatial domain. Two spatial domains are examined: one is the total model cross-sectional area, and the other is limited to a central strip, $|x| \le 1\,\mathrm{km}$, within which the frontogenesis occurs and where there is much less evolutionary change in $h(x, t)$ (Fig. 12). In both domains, $\mathcal{R}(t)$ rapidly rises (within the first $\Delta t \approx 0.03$ days) to a value of about 0.2 and then fluctuates about this value for the rest of the integration, even beyond the time of maximum central downwelling ($t = 0.65$ days). The spatial pattern of $\mathbf{u}_\perp^{\mathrm{TTW}} - \mathbf{u}_\perp$ is somewhat complex and generally on a smaller scale than the filament fields as a whole. A large part of it reflects the finite acceleration $\partial_t \mathbf{u}_\perp$ in the momentum balance because of the rather rapid frontogenetic evolution of the filament. Separate plots of $\mathbf{u}_\perp^{\mathrm{TTW}}(x, z)$ and $\mathbf{u}_\perp(x, z)$ show a strong resemblance at all times, but they are not included here. Therefore, we conclude that TTW balance is fairly well, but not perfectly, maintained by a continuing adjustment process during the frontogenesis.

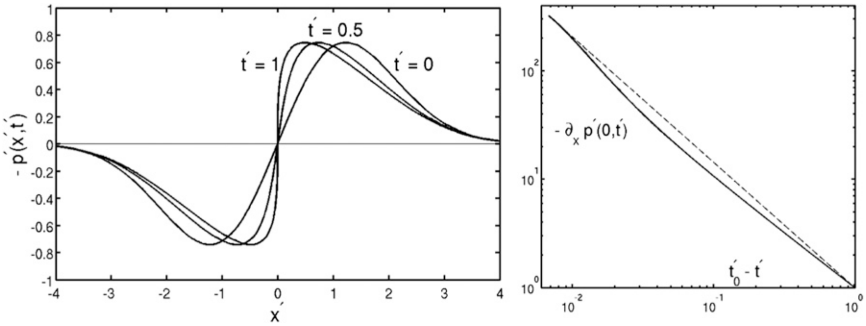

FIG. 14. An approximate numerical solution $p'(x', t')$ of (19) with (22) and Pe $= \infty$. (left) $-p'(x')$ at $t' = 0$, 0.5, and 1.0, showing the progression toward a positive-step discontinuity at $x' = 0$. (right) $-\partial_{x'}p'(0, t')$ vs $t'_0 - t'$ (solid line) for a value of $t'_0 = 1.008$, which is determined to make the result approximately fit (23) (dashed line) on this log–log plot over the interval $0 \le t' \le 1.0$, indicative of a finite-time singularity in the derivative of p'.

6. An approximate model for filament frontogenesis

Consider the buoyancy equation in 2D with vertical and horizontal mixing:

$$\partial_t b = -u\partial_x b - w\partial_z b + \partial_z(\kappa_v \partial_z b) + \kappa_\perp \partial_x^2 b. \quad (17)$$

Within the mixed layer near the surface, $\partial_z b$ is very small, so the second and third right-side terms can be neglected. If an approximate TTW balance is assumed and if the Ekman velocity from τ^s is neglected, then from (7)

$$u(\eta) \approx -\frac{Sh}{2},$$

where h is a boundary layer depth scale and $\partial_x b = Sf$. Substituting this into (17) gives an approximate evolution equation for b near the surface:

$$\partial_t b = \frac{C}{2}(\partial_x b)^2 + \kappa_\perp \partial_x^2 b,$$

with $C = h/f$, or by taking another derivative in x and defining $p = \partial_x b$,

$$\partial_t p = Cp\partial_x p + \kappa_\perp \partial_x^2 p. \quad (18)$$

Nondimensionalize p, t, and x by p_0, t_0, and ℓ_0 to finally obtain

$$\partial_{t'} p' + p'\partial_{x'} p' = \frac{1}{\mathrm{Pe}}\partial_{x'}^2 p' \quad (19)$$

when the following choices are made:

$$p_0 = -Sf, \quad t_0 = \frac{\ell_0}{Sh}, \quad \mathrm{Pe} = \frac{Sh\ell_0}{\kappa_\perp}. \quad (20)$$

Primes denote nondimensional variables. Equation (19) is Burgers' equation in 1D where Pe is the Peclet number. For large Pe (small diffusion), solutions of Burgers' equation are mathematically known to evolve toward discontinuous solutions in x (i.e., shocks) in finite time (Hopf 1950; Whitham 1974). For finite but large Pe, a near-shock solution will approximately locally equilibrate with a finite width scale:

$$\ell_e \sim \kappa_\perp / Sh, \quad (21)$$

which is smaller as the buoyancy gradient and/or boundary layer depth are larger or as the horizontal diffusivity is smaller; on a longer time scale, the solution will diffusively decay. In the filament evolution solutions in section 5, neither S nor h change very much with time, and hence ℓ_e is approximately known from $\kappa_\perp$ and the filament initial conditions.

To illustrate this behavior with relevance to the filament frontogenesis in section 5, consider an initial-value problem for (19) with

$$p'(x, 0) = -x'e^{-(x'^2)/3}. \quad (22)$$

This has the same general shape as $-\partial_x b(x, 0, 0)$ for a dense filament as in (8) and Fig. 5, here with a somewhat broader far-field decay scale; the important region for the shock development is the neighborhood of $x' = 0$. This is evident in Fig. 14: $p'(x)$ evolves toward a discontinuity at $x' = 0$, and its derivative evolves toward a singularity at a finite time, that is, with a functional dependence in the form of

$$\partial_{x'} p'(0, t') \sim \frac{c_0}{(t'_0 - t')^\alpha} \quad (23)$$

locally in time close to the singularity at $t' = t'_0$. For this solution, a global fit in time (for simplicity) yields estimated values of $t'_0 \approx 1.008$, $c_0 \approx -1.008$, and $\alpha \approx 1.16$, and this fit is also plotted in Fig. 14 (right).[2] Although the fit is imperfect for this particular numerical solution, and an accurate numerical solution approaching a singularity is difficult, and nevertheless the result is highly suggestive of the theoretically expected singular behavior.

Burgers' equation has been identified before in theoretical analyses of strain-induced frontogenesis for an atmospheric surface front in the specific context of the Hoskins and Bretherton (1972) model (Blumen 1980; Boyd 1992)[3] but not for the TTW-induced phenomenon examined here. As here, however, their primary result was a finite-time singularity in an inviscid balanced model of frontogenesis.

In summary, the approximate model system (18) indicates an evolution of $\partial_x b$ near the surface in a dense/cold filament toward a horizontal positive-step discontinuity until limited by diffusive processes; furthermore, with the assumption of TTW balance (section 3), $b(x, z)$ will evolve toward a negative cusp at the center, $u(x, z)$ and $v(x, z)$ will evolve toward opposite-sign discontinuities, and ζ will evolve toward a cyclonic singularity—all of which are qualitatively consistent with the full-system evolution in section 5 up to the time limit of computational reliability (i.e., $t = 0.65$ days). This behavior is analogous to the finite-time singularity for the strain-induced frontogenesis of a semigeostrophically balanced front with uniform interior potential vorticity and conservative dynamics (Hoskins and Bretherton 1972). These singularities are unlikely to be realized for the actual frontal or filament evolution because the balance approximations are unlikely to be exact (see the end of section 5b), small-scale 3D instabilities are likely to arise, and the fluid is not inviscid.

7. Summary and prospects

In the presence of turbulent momentum mixing in the surface boundary layer, a dense filament structure in $b(x, z)$ develops a momentum-balanced circulation, the turbulent thermal wind (TTW). (Without the presence of turbulence, the momentum balance would simply be geostrophic, and no further evolution need occur.) In the cross-filament plane, the secondary circulation has surface horizontal convergence with downwelling underneath (section 3). This leads to a frontogenetic sharpening of the central horizontal shear of the down-filament velocity, that is, the vertical vorticity, with accompanying sharpening in the surface convergence pattern, vertical velocity, and density curvature (section 5b). In an approximate model of the surface buoyancy evolution assuming TTW balance (section 6), the advective tendency of the convergent secondary circulation leads to a finite-time singularity in the central vorticity ζ, although of course this is not demonstrable in a full 2D hydrostatic computational integration that has more general dynamics than just the TTW balance and has a diffusive regularization near the grid scale necessary to avoid computational blowup.

The frontogenesis is a result of the surface geostrophic vertical shear $S_g = \partial_z v_g$ and the boundary layer turbulent mixing ν_v. Approximate scaling relations, derived from the TTW model (section 3) and the frontogenesis model (section 6), are that the ageostrophic shear is comparable to the geostrophic shear $S_a \sim S_g$; the time to develop significant frontogenesis is the advective time $t_0 \sim \ell_0/S_g h \sim \zeta_g^{-1}$; and, in the presence of a horizontal eddy diffusion process, the possible horizontal frontal arrest scale is $\ell_e \sim \kappa_\perp/S_g h \sim \kappa_\perp/(\ell_0 \zeta_g)$, or when $\ell_0 \rightarrow \ell_e$ and $\zeta_g \rightarrow \zeta_e$ (an equilibrated value), $\ell_e \rightarrow \sqrt{\kappa_\perp/\zeta_e}$. Although the existence of a significant ν_v is a necessary enabler of the frontogenesis, the evolution itself is not a sensitive function of its value.

Thus, the general picture is that seed density filaments are created in the midst of chaotic horizontal advection by mesoscale eddies; they are sometimes frontogenetically sharpened into strong submesoscale filaments by further mesoscale straining deformation; and they will further evolve frontogenetically by the interaction of boundary layer turbulence with the filament density structure that maintains the TTW secondary circulation. Analogous phenomena occur for surface density fronts: a mixing-induced secondary circulation qualitatively similar to the one induced by straining deformation and a frontogenetic tendency on the dense, cyclonic, downwelling side of the front where the surface horizontal velocity is convergent.

The solutions presented here call for further consideration of how to parameterize boundary layer turbulence in submesoscale circulation regimes where the space–time scale gap is not large (i.e., kilometers or less horizontally, tens of meters vertically, and multiple hours temporally). The widely used K-profile parameterization

[2] The time to reach the first singularity is analytically calculable from the initial profile $p'(x, 0)$ by using the method of characteristics for Burgers' equation, as explained in Boyd (1992).

[3] Blumen (1980) even anticipated the TTW effect in a front by appending a surface Ekman layer to the inviscid model of Hoskins and Bretherton (1972). A "vertical velocity jet" through the cyclonic vorticity part of the front was noted, which is a part of the TTW secondary circulation. However, the frontogenetic effect was not part of his particular solution, although he did comment that "convergence in the boundary layer should tend to concentrate gradients of wind and temperature, while the divergent flow aloft would be frontolytic" (Blumen 1980, p. 76), which was prescient but not followed through on.

(KPP) boundary layer scheme in its native form evinces fine structure not generally present in applications for larger-scale circulation; here, it turns into an unintended stochastic parameterization at least on the sides of the filament. The most plausible step forward is to inculcate finite horizontal and temporal correlation scales presently missing in the KPP scheme, as has been done provisionally simply by limiting the rate of change of h in (15). There is the further implication from the utility of V_0 in maintaining a deeper boundary layer on the flanks of the evolving filament (section 5a) that additional turbulent energy generation and pycnocline entrainment processes may become active in a submesoscale environment through additional turbulence generation in the large "mean" shears that are present. The central filament zone does not exhibit this fine structure delicacy in its KPP fields (h, ν_v, and κ_v) even without finite values of V_0 or t_*; hence, the central filament frontogenesis prediction seems robust within models of this class or even, one could extrapolate, eddy viscosity models in general. However, the general subject of boundary layer–submesoscale interactions needs further exploration. The most reliable tool for this exploration would be a nonhydrostatic large-eddy simulation that resolves both flow components with only mild parameterization assumptions. Finally, the present 2D solutions preclude 3D instability processes—especially the barotropic instability of the developing vortex sheet in the filament center, which is the primary instability mode for Gulf Stream filaments (Gula et al. 2014)—that may interrupt or even arrest the frontogenetic progression or at least transform it into more fragmented surface vorticity lines; this too warrants further exploration.

Acknowledgments. This research is sponsored by the Office of Naval Research (N00014-11-1-0726, N00014-12-1-0939, and N00014-12-1-0105) and National Science Foundation (DMS-0723757 and OCE-1049134). Insightful comments by anonymous reviewers are appreciated.

APPENDIX

TTW Solver in ROMS

For reproducibility, the discretization of the TTW algorithm in ROMS is included.

ROMS has a staggered grid (Shchepetkin and McWilliams 2005). In the vertical the horizontal velocity $\mathbf{u}_k$ and dynamic geopotential ϕ_k, $k = 1, \ldots, N$, are located at cell centers with thickness H_k such that $\sum_1^N H_k = H + \eta$, the ocean column depth. The vertical viscosity $\nu_{vk+1/2}$, $k = 1, \ldots, N-1$, is located at interior cell interfaces. The geopotential φ is obtained hydrostatically by vertical integration of b with a surface boundary condition equal to $g\eta$.

The discrete TTW problem for $\mathbf{u}_\perp(z)$ is posed in ROMS as the horizontal momentum balance—rather than as its vertical derivative in (1)–(4)—at the vertical cell centers. For interior cells, $k = 2, \ldots, N-1$, the equations are

$$\begin{aligned}
-fH_k v_k &= -H_k(\partial_x\phi)_k + [A_{k+1/2}(u_{k+1} - u_k) \\
&\quad - A_{k-1/2}(u_k - u_{k-1})] \\
fH_k u_k &= -H_k(\partial_y\phi)_k + [A_{k+1/2}(v_{k+1} - v_k) \\
&\quad - A_{k-1/2}(v_k - v_{k-1})],
\end{aligned} \tag{A1}$$

where $A_{k+1/2} = 2\nu_{vk+1/2}/(H_k + H_{k+1})$, $k = 1, \ldots, N-1$ are the viscous flux factors between adjacent grid cells. They need not be defined at the surface and bottom because they are replaced by the boundary conditions at $z = -H$ and η. In the top cell, the second right-side terms are replaced by the surface wind stresses τ^{sx}/ρ_0 and τ^{sy}/ρ_0, respectively. In the bottom cell, $k = 1$, the final right-side terms are zero because of zero stress at $z = -H$. (Its generalization to a nonzero bottom stress would be analogous to the surface stress replacement.) This system is rewritten for $k = 2, \ldots, N-1$ as

$$\mathbf{a}_{k-1/2}\mathbf{u}_{k-1} + \mathbf{b}_k\mathbf{u}_k + \mathbf{a}_{k+1/2}\mathbf{u}_{k+1} = \mathbf{d}_k, \tag{A2}$$

where the two vectors are the velocity and pressure gradient

$$\mathbf{u}_k = \begin{pmatrix} u_k \\ v_k \end{pmatrix} \quad \text{and} \quad \mathbf{d}_k = -\begin{bmatrix} H_k(\partial_x\phi)_k \\ H_k(\partial_y\phi)_k \end{bmatrix}, \tag{A3}$$

and the 2×2 matrices are

$$\mathbf{a}_{k\pm1/2} = -\begin{pmatrix} A_{k\pm1/2} & 0 \\ 0 & A_{k\pm1/2} \end{pmatrix} \quad \text{and}$$

$$\mathbf{b}_k = \begin{pmatrix} A_{k+1/2} + A_{k-1/2} & -fH_k \\ fH_k & A_{k+1/2} + A_{k-1/2} \end{pmatrix}. \tag{A4}$$

As explained above, the analogous forms of (A2) at the boundary-adjacent cells are altered to include the boundary conditions at $k = 1$ the terms involving $A_{k-1/2}$ through $\mathbf{a}_{k-1/2}$ and $\mathbf{b}_k$ are replaced by zero, and at $k = N$, the terms involving $A_{k-1/2}$, $\mathbf{a}_{k-1/2}$, and $\mathbf{b}_k$ are replaced by the vector

$$-\begin{pmatrix} \tau^{sx}/\rho_0 \\ \tau^{sy}/\rho_0 \end{pmatrix}, \tag{A5}$$

which can be moved to the right side as an additional forcing term.

This system [(A2)] for $k = 1, \ldots, N$ has a block tridiagonal matrix for the $2N$ velocities (u_k, v_k). The block Gaussian elimination procedure algorithmically follows the standard Gaussian elimination (e.g., section 8.5 in Richtmeyer and Morton 1967), where the system is first brought into the upper (or lower) two-diagonal form, starting from one side (as the boundary equations already exist as relations between just two neighboring unknowns), followed by the back substitution sweep. The only difference between the block and the standard procedure is that now instead of scalar variables, we operate with two vectors and 2×2 matrices, and division by the middle coefficient during forward sweep is replaced with inversion of the 2×2 matrix performed at every index k.

Given $\mathbf{u}_\perp$ and η, w is calculated from the continuity relation as usual in ROMS.

Obviously, the TTW system for $\mathbf{s} = \partial_z \mathbf{u}_\perp$ in (1)–(4) is fully equivalent to the continuous system solved here for $\mathbf{u}_\perp$, and discrete solutions can be (and were) obtained for either system.

REFERENCES

Blumen, W., 1980: A comparison between the Hoskins-Bretherton model of frontogenesis and the analysis of an intense frontal zone. *J. Atmos. Sci.,* **37,** 64–77, doi:10.1175/1520-0469(1980)037<0064:ACBTHB>2.0.CO;2.

Boyd, J., 1992: The energy spectrum of fronts: Time evolution of shocks in Burgers' equation. *J. Atmos. Sci.,* **49,** 128–139, doi:10.1175/1520-0469(1992)049<0128:TESOFT>2.0.CO;2.

Capet, X. J., J. C. McWilliams, M. J. Molemaker, and A. F. Shchepetkin, 2008a: Mesoscale to submesoscale transition in the California Current System. Part I: Flow structure, eddy flux, and observational tests. *J. Phys. Oceanogr.,* **38,** 29–43, doi:10.1175/2007JPO3671.1.

——, ——, ——, and ——, 2008b: Mesoscale to submesoscale transition in the California Current System. Part II: Frontal processes. *J. Phys. Oceanogr.,* **38,** 44–64, doi:10.1175/2007JPO3672.1.

Davidson, P. A., 2004: *Turbulence: An Introduction for Scientists and Engineers.* Oxford University Press, 657 pp.

Garrett, C., and J. Loder, 1981: Dynamical aspects of shallow sea fronts. *Philos. Trans. Roy. Soc. London,* **B302,** 563–581, doi:10.1098/rsta.1981.0183.

Gula, J., M. J. Molemaker, and J. C. McWilliams, 2014: Submesoscale cold filaments in the Gulf Stream. *J. Phys. Oceanogr.,* **44,** 2617–2643, doi:10.1175/JPO-D-14-0029.1.

Hakim, G., C. Snyder, and D. Muraki, 2002: A new surface model for cyclone–anticyclone asymmetry. *J. Atmos. Sci.,* **59,** 2405–2420, doi:10.1175/1520-0469(2002)059<2405:ANSMFC>2.0.CO;2.

Hopf, E., 1950: The differential equation $u_t + uu_x = u_{xx}$. *Commun. Pure Appl. Math.,* **3,** 201–230, doi:10.1002/cpa.3160030302.

Hoskins, B. J., 1982: The mathematical theory of frontogenesis. *Annu. Rev. Fluid Mech.,* **14,** 131–151, doi:10.1146/annurev.fl.14.010182.001023.

——, and F. P. Bretherton, 1972: Atmospheric frontogenesis models: Mathematical formulation and solution. *J. Atmos. Sci.,* **29,** 11–37, doi:10.1175/1520-0469(1972)029<0011:AFMMFA>2.0.CO;2.

Lapeyre, G., and P. Klein, 2006: Impact of the small-scale elongated filaments on the oceanic vertical pump. *J. Mar. Res.,* **64,** 835–851, doi:10.1357/002224006779698369.

Large, W. G., J. C. McWilliams, and S. C. Doney, 1994: Oceanic vertical mixing: A review and a model with a nonlocal boundary layer parameterization. *Rev. Geophys.,* **32,** 363–403, doi:10.1029/94RG01872.

McWilliams, J. C., and M. J. Molemaker, 2011: Baroclinic frontal arrest: A sequel to unstable frontogenesis. *J. Phys. Oceanogr.,* **41,** 601–619, doi:10.1175/2010JPO4493.1.

——, ——, and E. I. Olafsdottir, 2009a: Linear fluctuation growth during frontogenesis. *J. Phys. Oceanogr.,* **39,** 3111–3129, doi:10.1175/2009JPO4186.1.

——, F. Colas, and M. J. Molemaker, 2009b: Cold filamentary intensification and oceanic surface convergence lines. *Geophys. Res. Lett.,* **36,** L18602, doi:10.1029/2009GL039402.

——, E. Huckle, and A. F. Shchepetkin, 2009c: Buoyancy effects in a stratified Ekman layer. *J. Phys. Oceanogr.,* **39,** 2581–2599, doi:10.1175/2009JPO4130.1.

——, ——, J.-H. Liang, and P. P. Sullivan, 2014: Langmuir turbulence in swell. *J. Phys. Oceanogr.,* **44,** 870–890, doi:10.1175/JPO-D-13-0122.1.

Munk, W., L. Armi, K. Fischer, and F. Zachariasen, 2000: Spirals on the sea. *Proc. Roy. Soc. London,* **A456,** 1217–1280, doi:10.1098/rspa.2000.0560.

Nagai, T., A. Tandon, and D. L. Rudnick, 2006: Two-dimensional ageostrophic secondary circulation at ocean fronts due to vertical mixing and large-scale deformation. *J. Geophys. Res.,* **111,** C09038, doi:10.1029/2005JC002964.

Ponte, A., P. Klein, X. Capet, P.-Y. Le Traon, B. Chapron, and P. Lherminier, 2013: Diagnosing surface mixed layer dynamics from high-resolution satellite observations: Numerical insights. *J. Phys. Oceanogr.,* **43,** 1345–1355, doi:10.1175/JPO-D-12-0136.1.

Richtmeyer, R. D., and K. W. Morton, 1967: *Difference Methods for Initial Value Problems.* Wiley, 405 pp.

Rudnick, D., 1996: Intensive surveys of the Azores Front: 2. Inferring the geostrophic and vertical velocity fields. *J. Geophys. Res.,* **101,** 16 291–16 303, doi:10.1029/96JC01144.

——, and J. Luyten, 1996: Intensive surveys of the Azores Front: 1. Tracer and dynamics. *J. Geophys. Res.,* **101,** 923–939, doi:10.1029/95JC02867.

Shchepetkin, A. F., and J. C. McWilliams, 2005: The Regional Oceanic Modeling System (ROMS): A split-explicit, free-surface, topography-following-coordinate ocean model. *Ocean Modell.,* **9,** 347–404, doi:10.1016/j.ocemod.2004.08.002.

——, and ——, 2008: Computational kernel algorithms for finescale, multi-process, long-time oceanic simulations. *Handb. Numer. Anal.,* **14,** 121–183, doi:10.1016/S1570-8659(08)01202-0.

Thomas, L., and C. Lee, 2005: Intensification of ocean fronts by down-front winds. *J. Phys. Oceanogr.,* **35,** 1086–1102, doi:10.1175/JPO2737.1.

Whitham, G. B., 1974: *Linear and Nonlinear Waves.* Wiley, 636 pp.